Compact group analysis using weak gravitational lensing

Martín Chalela,[1,2]★ Elizabeth Johana Gonzalez,[1,2,3] Diego Garcia Lambas[1,3]
and Gael Foëx[4]

[1]*Instituto de Astronomía Teórica y Experimental (IATE-CONICET), Laprida 854, X5000BGR Córdoba, Argentina*
[2]*Facultad de Matemática, Astronomía y Física, FAMAF, Universidad Nacional de Córdoba, X5000BGR Córdoba, Argentina*
[3]*Observatorio Astronómico de Córdoba, Universidad Nacional de Córdoba, Laprida 854, X5000BGR Córdoba, Argentina*
[4]*Max Planck Institute for Extraterrestrial Physics, Giessenbachstrasse, D-85748 Garching, Germany*

ABSTRACT

We present a weak lensing analysis of a sample of Sloan Digital Sky Survey compact groups (CGs). Using the measured radial density contrast profile, we derive the average masses under the assumption of spherical symmetry, obtaining a velocity dispersion for the singular isothermal spherical model, $\sigma_V = 270 \pm 40 \, \mathrm{km \, s^{-1}}$, and for the NFW model, $R_{200} = 0.53 \pm 0.10 \, h_{70}^{-1} \, \mathrm{Mpc}$. We test three different definitions of CG centres to identify which best traces the true dark matter halo centre, concluding that a luminosity-weighted centre is the most suitable choice. We also study the lensing signal dependence on CG physical radius, group surface brightness and morphological mixing. We find that groups with more concentrated galaxy members show steeper mass profiles and larger velocity dispersions. We argue that both, a possible lower fraction of interloper and a true steeper profile, could be playing a role in this effect. Straightforward velocity dispersion estimates from member spectroscopy yield $\sigma_V \approx 230 \, \mathrm{km \, s^{-1}}$ in agreement with our lensing results.

Key words: gravitational lensing: weak – galaxies: groups: general.

1 INTRODUCTION

The largest concentrations of mass and visible matter in the Universe reside in galaxy clusters. However, a significant fraction of galaxies are located in groups of different mass and morphology content (Karachentsev 2005). Studying the physical properties of these systems is of prime importance to understand galaxy formation and evolution.

Compact groups (CGs) of galaxies are a special class of galaxy systems, containing generally four to six members within a region of just a few galaxy radii, and with a low radial velocity dispersions ($\sim$200 km s^{-1}; e.g. McConnachie et al. 2009). This particular combination implies that CGs have short crossing times ($\sim$0.2 Gyr), providing an ideal scenario to study galaxy merging and the impact of environment on galaxy evolution. However, the effects of such an extreme environment and the short time-scales in which these systems would collapse are not completely understood, setting an ongoing debate about the nature of these systems. Numerical simulations have shown that member galaxies can eventually merge and so groups may disappear (Barnes 1985, 1989; Mamon 1987) in a time-scale comparable to the observed crossing times (Hickson et al. 1992). Other simulations present an alternative picture, where CG lifetime is much longer than the crossing time (Governato, Bha-

tia & Chincarini 1991; Athanassoula, Makino & Bosma 1997) that would explain the relatively high number density of these systems in the observations. Nevertheless, there is a strong debate regarding the genuineness of these systems, since it has been suggested that most of them could be spurious line-of-sight alignments rather than truly bound systems (Mamon 1986).

In a widely accepted scenario, CGs are gravitationally bound, but unstable systems. The X-ray observations showing great emission from the hot intragroup gas (Ponman et al. 1996) suggest that strong interactions between member galaxies could have provided a significant intragroup medium. Orbital decay due to dynamical friction should strip away galaxies from their haloes resulting in eventual mergers in short time-scales, leading to a morphological evolution. Therefore, the fraction of early-type galaxies would pinpoint the evolutionary state of the groups as a whole. Although group members can merge, CGs may increase their number of members by acquiring them from the surroundings, extending their lifetime (Diaferio, Geller & Ramella 1994). Many studies support this scenario showing that most of these galaxy systems reside within larger structures such as loose groups and rich clusters (e.g. Rood & Struble 1994; de Carvalho et al. 2005; Mendel et al. 2011).

Hickson CG (hereafter HCG; Hickson 1982) sample has been widely analysed providing several studies of these systems at low redshift ($z \sim 0.03$). High mass-to-light ratio determinations of $50 \, h \, \Upsilon_{\odot}$ and typical line-of-sight velocity dispersions of 200 km s^{-1}

(Hickson et al. 1992) suggest the presence of substantial amounts of dark matter. Furthermore, a recent study by Pompei & Iovino (2012), based on spectroscopically confirmed CGs at higher redshift ($z \sim 0.12$), reports remarkably higher average values of $M/L_B = 190\,\Upsilon_\odot$ and $\sigma_{LOS} = 273\,\mathrm{km\,s^{-1}}$. The authors suggest that these high values could be due to the proximity of large-scale structures, which may affect mass estimates. Despite differences with other authors, these results are consistent with predictions of the hierarchical model of structure formation. Results from hydrodynamical and *N*-body simulations show that individual dark matter haloes of CG members merge first, creating a common massive halo that dominates galaxy dynamics (Barnes 1984; Bode, Cohn & Lugger 1993).

Until now CGs' masses have been determined through a dynamical approach, either by measuring velocity dispersions or through X-ray observations. Ponman et al. (1996) showed that these systems slightly deviate from the known relation L_X–T for clusters (being fainter than the predicted one) but are still consistent with the L_X–σ_{LOS} relation. Gravitational lensing provides an alternative approach to measure the mass of galaxy systems. Mendes de Oliveira & Giraud (1994) analysed the possibility that a CG could act as a lensing system. Based on the HCGs, the authors quantified the lensing efficiency, concluding that they would be too weak to be detected as a lens since this sample is quite nearby. However, their calculations show that CGs at higher redshifts ($z \sim 0.1$), such as those available in modern catalogues, could produce a detectable lensing signal.

Weak lensing techniques have been applied almost exclusively to clusters of galaxies providing precise determinations consistent with values derived from dynamical analysis and X-ray observations (Hoekstra et al. 1998; Fischer 1999; Clowe et al. 2000). In recent years, several studies have analysed the lensing effects produced by groups of galaxies (e.g. George et al. 2012; Spinelli et al. 2012; Foëx et al. 2013, 2014); nevertheless, none of them have focused on CGs. In order to apply weak lensing techniques to low-mass galaxy systems, such as groups with masses $\sim 10^{13}\,\mathrm{M_\odot}$, stacking techniques have shown to be a powerful tool to increase the signal-to-noise ratio (S/N) and thus, suitable to derive groups' statistical properties (e.g. Rykoff et al. 2008; Leauthaud et al. 2010; Foëx et al. 2014).

In this work, we present the first statistical weak lensing analysis of a sample of CGs using stacking techniques. Our systems were extracted from the catalogue of CGs of McConnachie et al. (2009). Images for the analysis were obtained from Sloan Digital Sky Survey (SDSS) data (York et al. 2000). This survey has the largest imaging coverage available at present, providing a statistically significant data base suitable for stacking techniques. These data have been successfully used in previous weak lensing studies to analyse the density profile and determine total masses of galaxies and galaxy systems (e.g. Mandelbaum et al. 2006; Sheldon et al. 2009; Clampitt & Jain 2016; Gonzalez et al. 2016). From our lensing analysis, we derive the average mass under the assumption of spherical symmetry. We probe three different definitions of CG centre to identify which one best traces the dark matter halo. Furthermore, we compare our results with dynamical estimates, and we analyse the observed lensing signal according to various CG properties. The paper is organized as follows. In Section 2, we describe the selection of groups used throughout the study. In Section 3, we briefly describe the weak lensing analysis, as this was extensively discussed in previous works, along with the formalism of miscentred density profiles. In Section 4, we present the obtained mass and finally, in Section 5 we summarize our results and compare them with other

studies. We adopt, when necessary, a standard cosmological model $H_0 = 70\,\mathrm{km\,s^{-1}\,Mpc^{-1}}$, $\Omega_m = 0.3$ and $\Omega_\Lambda = 0.7$.

2 CGS: SAMPLE DESCRIPTION AND SOURCE GALAXIES

2.1 McConnachie CGs

There are several catalogues of CGs in the literature. In general, the identification of these data sets follows Hickson's original selection criteria, or variations in order to identify similar systems. Some are based on spectroscopic information like Barton et al. (1996) and Allam & Tucker (2000), while others follow photometric criteria such as Hickson (1982), Prandoni, Iovino & MacGillivray (1994), Iovino (2002) and McConnachie et al. (2009). In order to statistically increase the lensing signal, the weak lensing analysis requires stacking of a large number of CGs. We have used McConnachie et al. (2009) catalogue, which comprises the largest CG sample available at present. This catalogue is based on photometric data from the sixth data release of SDSS (SDSS-DR6; Adelman-McCarthy et al. 2008). CGs were identified by applying Hickson (1982) criteria, where member galaxies satisfy

  (i) $N(\Delta m = 3) \geq 4$;
  (ii) $\theta_N \geq 3\theta_G$;
  (iii) $\mu \leq 26.0\,\mathrm{mag\,arcsec^{-2}}$.

$N(\Delta m = 3)$ is the number of member galaxies within 3 mag of the brightest galaxy, θ_G is the angular diameter of the smallest circle that encloses the centres of these galaxies, θ_N is the angular diameter of the largest concentric circle with no additional galaxy in this magnitude range or brighter and μ is the effective surface brightness of member galaxies (where the total flux is averaged over the circle of angular diameter θ_G).

These criteria were applied in two ranges of limiting magnitude resulting in two data sets, catalogue A and catalogue B. Catalogue A includes 2297 CGs identified from galaxies with *r* magnitude in the range $14.5 \leq r \leq 18.0$. Catalogue B contains 74 791 CGs with member galaxies in a wider magnitude range $14.5 \leq r \leq 21.0$. An individual visual inspection of all groups in catalogue A was carried out minimizing the contamination of the sample due to photometric errors in the automatic SDSS pipelines. This procedure was not applied to catalogue B given the large number of objects, with an estimated contamination by false sources of about 14 per cent. Both catalogues provide detailed information about CGs and their member galaxies such as group surface brightness, radius and number of members, as well as each galaxy *r* and *g* magnitude, and spectroscopic redshift (when available). Given that the Hickson criterion relies only on photometric information, not all CG members may have spectroscopic data.

2.2 Final sample and image data

For statistical reasons, we extracted our sample from catalogue B. Redshifts of all galaxies in this catalogue were updated with information from SDSS Data Release 12 (Alam et al. 2015; http://www.sdss.org/dr12/), and we recalculated CG redshifts as the mean value of the group members. The redshift distribution of the updated catalogue B peaks at $z \approx 0.1$ extending up to $z \approx 0.6$.

Given that the lensing efficiency depends on the lens distance and considering that the redshift distribution peaks at $z \sim 0.1$, we discard groups with $z < 0.06$ that contribute little weight. We also
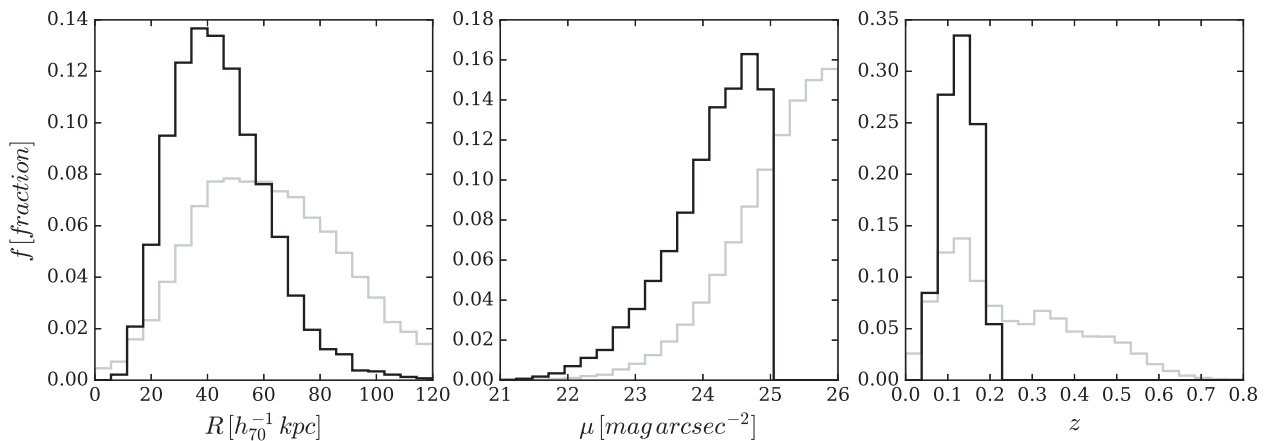
Figure 1. Normalized distributions of parameters of the analysed CGs (black line) and catalogue B (grey line). From left to right: physical radius R, surface brightness μ and redshift z.

discard systems with $z > 0.2$ since the density of background galaxies is insufficient to extract a reliable signal. We analyse only objects with $\mu \leq 25$ mag arcsec^{-2}, where μ is defined as the r-band surface brightness. This cut is made to increase the fraction of CGs without interlopers in the sample; members of brighter groups are more probable to be part of a real bound system and not a visual alignment in the sky. According to McConnachie, Ellison & Patton (2008), the sample purity improves from about 30 per cent, for CGs with $\mu \leq 26$ mag arcsec^{-2}, to 43 per cent, for groups with $\mu \leq 25$ mag arcsec^{-2}.

The final sample consists of 6257 CGs. In Fig. 1, we show the distribution of CG properties of catalogue B and our final sample. It can be noticed that with the mentioned cuts, we exclude the more extended ($R \gtrsim 80\, h_{70}^{-1}$ kpc) CGs.

Image data were obtained from the SDSS. This survey provides the largest photometric and spectroscopic public data base available at present. It was constructed using a 2.5 m telescope at Apache Point Observatory in New Mexico. The 10th data release (SDSS-DR10; Ahn et al. 2014; http://www.sdss.org/dr10/) covers 14 555 square degrees of sky imaged in five bands (u, g, r, i and z) and has a limiting magnitude $r = 22.2$. For the lensing analysis, we use images in the r and i bands, obtained from DR10 as it includes all prior SDSS imaging data. This allows us to select the frame with the best seeing conditions in the field of a given CG. Each SDSS image is 9.8 arcmin × 13.5 arcmin, corresponding to 1489 × 2048 pixels, with a pixel size of 0.396 arcsec. The average seeing is about 1 arcsec in the i band.

2.3 Photometry, source classification and shape measurements

In this subsection, we describe the details regarding detection, classification and shape measurements of background galaxies. The implemented pipeline has been successfully applied to SDSS data in order to estimate total masses of galaxy systems (Gonzalez et al. 2016).

We conduct a search of frames in order to analyse the most adequate images for our lensing analysis. Thus, for each CG, we sequentially search and retrieve the best centred i-band frames within 50 pixels from the borders and select the first frame in the search with seeing lower than 0.9 arcsec. If no frame satisfies this seeing condition, we choose that with the lowest seeing, up to 1.3 arcsec. CGs in frames not satisfying seeing values <1.3 arcsec are discarded. This results in 5568 CGs suitable for the analysis (i.e. ~90 per cent of

the selected 6257 systems). After the i-band frame is selected, we also retrieve the corresponding r-band frame. Notice that given the low lensing signal expected at large radii from the lens centre, it is not necessary to use a frame mosaic, but rather use a single frame for each system.

To perform the detection and photometry of the sources, we implement SEXTRACTOR (Bertin & Arnouts 1996) as described in Gonzalez et al. (2015), in a two-pass mode. The first run is made with a detection level of 5σ above the background to detect bright objects and estimate the seeing. A second run is made with a detection level of 1.5σ in dual mode to detect objects on the i frame, while photometric parameters are measured on both i- and r-band frames.

Sources are classified in stars, galaxies and false detections according to their full-width at half-maximum (FWHM), stellarity index and position in the magnitude–peak surface brightness ($\mu_{\rm max}$) plot, where these parameters are obtained from SEXTRACTOR output. In Fig. 2, we show an example of the source classification for a single frame with seeing $=1.0$ arcsec. Objects that are more sharply peaked than the point spread function (PSF), thus with FWHM $<$ seeing -0.5 pixel, and with SEXTRACTOR FLAG parameter > 4, are considered as false detections. As the light distribution of a point source scales with magnitude, objects on the magnitude–$\mu_{\rm max}$ line ± 0.4 mag and FWHM $<$ seeing $+ 0.8$ pixel are considered as stars. The rest of the sources with stellarity index < 0.8 are classified as galaxies.

For the shape measurements, we use IM2SHAPE (Bridle et al. 2002) that computes the shape parameters modelling the object as a sum of Gaussians convolved with a PSF, also modelled as a sum of Gaussians. For simplicity, we modelled the sources and the PSF using only one Gaussian. The PSF map across the image is estimated from the shape of stars, since they are intrinsically point-like objects. We only used objects with a measured ellipticity smaller than 0.2 to remove most of the remaining false detections and faint galaxies. Looking at the five nearest neighbours of each star, we also removed those that differ by more than 2σ from the local average shape. Finally, the local PSF at each galaxy position is linearly interpolated by averaging the shapes of the five nearest stars. Once the PSF is determined, we run IM2SHAPE on galaxies to measure their intrinsic shape parameters. In order to test our PSF treatment, we apply the PSF correction on stars to check that it can recover point-like shapes. In Fig. 3, we show the major semi-axis distribution of stars for two frames, before and after taking into account the PSF in the shape measurement. After the PSF correction, the major semi-axis sizes
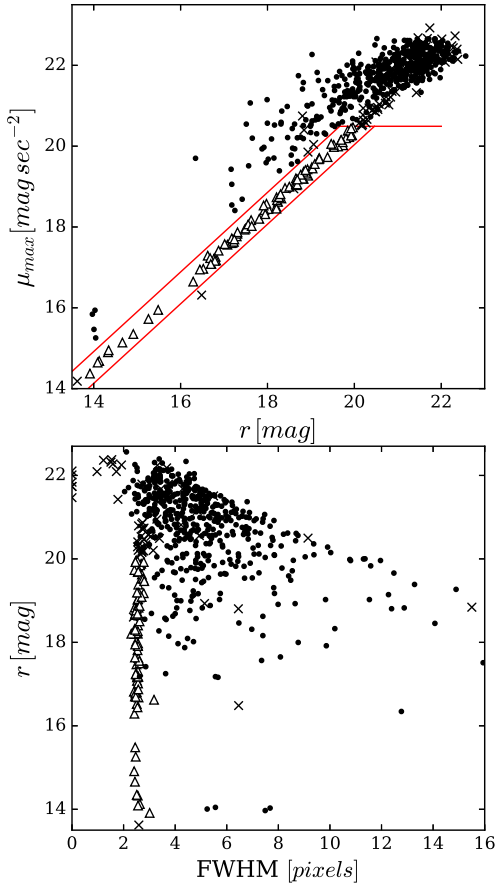
Figure 2. Source classification in a frame with seeing ≈1.0 arcsec. Stars and galaxies are represented with triangles and dots, respectively; false detections are marked with crosses. In the top panel, we show the magnitude–peak surface brightness scatter plots. Stars are located in the enclosed region (see the text) limited to a maximum μ_{max} value where galaxies start to overlap the star sequence. Sources at the fainter side of this region are considered as false detections. In the bottom panel, we show the FWHM–magnitude scatter plot.
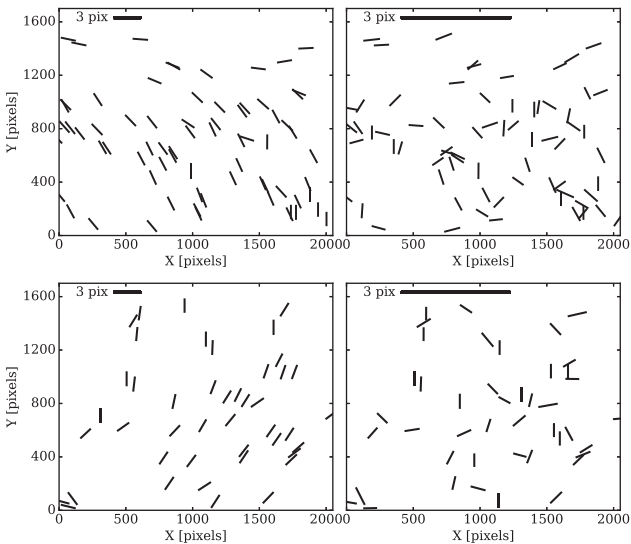

Figure 3. PSF correction applied to stars of two frames: semi-major axes before (left-hand panels) and after (right-hand panels) the deconvolution. Notice that after taking into account the PSF correction, semi-major axis orientations are randomly distributed and with significantly smaller moduli.
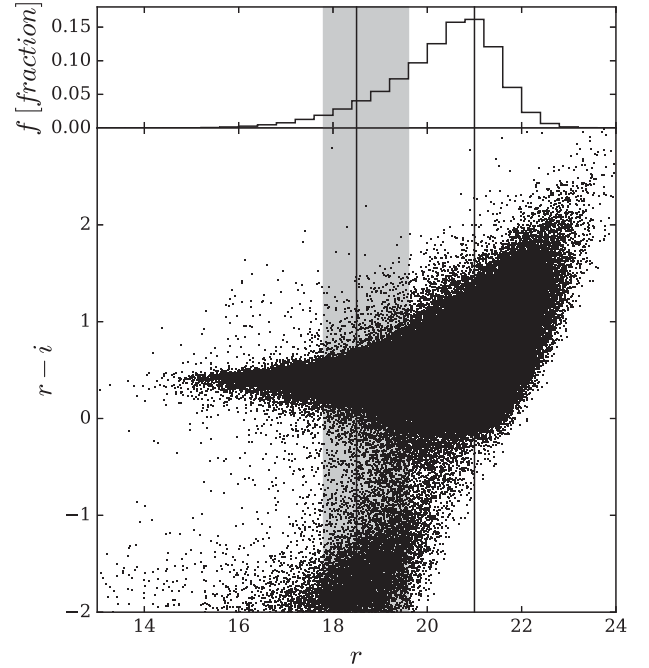
Figure 4. Colour–magnitude diagram (bottom) and normalized magnitude distribution (top) of sources classified as galaxies in the CG fields. The vertical lines indicate the magnitude cuts used for the selection of background galaxies. The shaded region spans the entire m_P range and the inner line indicates the mean value, $\langle m_P \rangle$. The solid line at $r = 21$ indicates the faint limit cut.

are considerably smaller and the orientation is randomly distributed, consistent with point-like sources.

To perform the lensing analysis, background galaxies are selected as those with r magnitudes between m_P and 21 mag. m_P is defined as the faintest magnitude at which the probability that a galaxy is behind the group is higher than 0.7. This value is computed according to the redshift of each CG using a catalogue of photometric redshifts (see Gonzalez et al. 2015, for details about m_P estimation). Discarding galaxies fainter than 21 mag ensures that we are not taking into account faint galaxies with high uncertainties in their shape measurements. We also restrict the selection to those objects with a good pixel sampling by using only galaxies with FWHM > 5 pixels. In Fig. 4, we show the colour–magnitude diagram of all selected galaxies with the photometric cuts used for the background galaxy selection. The average number of background galaxies obtained is 60 per frame, which corresponds to a density of ∼0.46 galaxies arcmin^{-2}, making a total of ∼2600 galaxies arcmin^{-2} for the catalogue used in the stacking analysis.

3 WEAK LENSING METHODOLOGY

3.1 Stacking technique

We briefly describe the lensing analysis and the stacking technique as these were described in detail in Gonzalez et al. (2015, 2016). Gravitational lensing effects are characterized by an isotropic stretching called convergence, κ, and an anisotropic distortion called shear, γ. Using the second derivative of the projected gravitational potential to express the shear and convergence, one can show that for a lens with a circular-symmetric projected mass distribution, the

tangential component of γ is related to the convergence through (Bartelmann 1995)

$$\gamma_{\mathrm{T}}(r) = \bar{\kappa}(< r) - \bar{\kappa}(r), \tag{1}$$

where $\bar{\kappa}(< r)$ and $\bar{\kappa}(r)$ are the convergence averaged over the disc and circle of radius r, respectively. On the other hand, the cross component of the shear, $\gamma_\times$, defined as the component tilted at $\pi/4$ relative to the tangential component, should be exactly zero.

Since the convergence is defined as the surface mass density $\Sigma(r)$ normalized by the critical density Σ_{crit}, we can rewrite the previous equation defining the density contrast, $\Delta\tilde{\Sigma}$, which is redshift independent:

$$\tilde{\gamma}_{\mathrm{T}}(r) \times \Sigma_{\mathrm{crit}} = \bar{\Sigma}(< r) - \bar{\Sigma}(r) \equiv \Delta\tilde{\Sigma}(r). \tag{2}$$

The tangential shear component is directly estimated as $\tilde{\gamma}_{\mathrm{T}} = \langle e_{\mathrm{T}} \rangle$, where the tangential ellipticity of background galaxies is averaged over annular bins. The averaged cross ellipticity component, in turn, should be zero and corresponds to the cross shear component.

For the composite lens, the density contrast is obtained as the weighted average of the tangential ellipticity of background galaxies:

$$\langle \Delta\tilde{\Sigma}(r) \rangle = \frac{\sum_{j=1}^{N_{\mathrm{Lens}}} \sum_{i=1}^{N_{\mathrm{Sources},j}} \omega_{ij} \times e_{\mathrm{T},ij} \times \Sigma_{\mathrm{crit},j}}{\sum_{j=1}^{N_{\mathrm{Lens}}} \sum_{i=1}^{N_{\mathrm{Sources},j}} \omega_{ij}}, \tag{3}$$

where ω_{ij} is the associated weight of each background galaxy as described in Gonzalez et al. (2016). N_{Lens} is the number of lensing systems and $N_{\mathrm{Sources},j}$ the number of background galaxies located at a distance $r \pm \delta r$ from the jth lens. $\Sigma_{\mathrm{crit},j}$ is the critical density for all the sources of the lens j, defined as

$$\Sigma_{\mathrm{crit},j} = \frac{c^2}{4\pi G} \frac{1}{\langle \beta_j \rangle D_{\mathrm{OL}_j}}.$$

Here D_{OL_j} is the angular diameter distance from the observer to the jth lens, G is the gravitational constant, c is the light velocity and $\langle \beta_j \rangle$ is the geometrical factor defined as the average ratio between the angular diameter distance from the galaxy source i to the lensing system j and the angular diameter distance between the observer and the source ($\langle \beta_j \rangle = \langle D_{\mathrm{LS}_j} / D_{\mathrm{OS}_i} \rangle_i$). Given the lack of redshift information for individual background galaxies, it is not possible to directly estimate the geometrical factor β. Therefore, we estimated this value using Coupon et al. (2009) catalogue of photometric redshifts. This catalogue is based on the public release Deep Field 1 of the Canada–France–Hawaii Telescope Legacy Survey, which is complete down to $m_r = 26$. We computed $\langle \beta_j \rangle$ after applying the same photometric cut used in the selection of background galaxies. This value is fairly insensitive to the detailed redshift distribution, as long as the mean redshift of background galaxies is considerably larger than the lens redshift (Meylan et al. 2006). This is the case of our sample, which has a mean redshift of 0.1, while the mean redshift of background galaxies is 0.32. We consider the contamination due to foreground galaxies by setting $\beta(z_{\mathrm{phot}} < z_{\mathrm{lens}}) = 0$, which outbalances the dilution of the shear signal by these unlensed galaxies. The average $\langle \beta_j \rangle$ value is ≈ 0.50.

The misidentification of faint group members as background galaxies weakens the lensing signal since they are not sheared. Although CGs have few members, numerical simulations suggest that fainter satellite galaxies could be surrounding the group. To overcome this problem, $\langle \Delta\tilde{\Sigma}(r) \rangle$ is multiplied by a factor $1 + f_{\mathrm{cg}}(r)$ following Hoekstra (2007), where $f_{\mathrm{cg}}(r)$ is the fraction of group members that remain in the catalogue of background galaxies. To estimate $f_{\mathrm{cg}}(r)$, we fit a $1/r$ profile to the galaxy excess relative to

the background level and we correct the measured shear according to the distance to the lensing system centre.

The statistical uncertainties associated with the estimator $\langle \Delta\tilde{\Sigma}(r) \rangle$ are computed taking into account the noise due to the galaxies' intrinsic ellipticity:

$$\sigma_{\Delta\tilde{\Sigma}}^2(r) = \frac{\sum_{j=1}^{N_{\mathrm{Lens}}} \sum_{i=1}^{N_{\mathrm{Sources},j}} (\omega_{ij} \times \sigma_\epsilon \times \Sigma_{\mathrm{crit},j})^2}{\left(\sum_{j=1}^{N_{\mathrm{Lens}}} \sum_{i=1}^{N_{\mathrm{Sources},j}} \omega_{ij} \right)^2}, \tag{4}$$

where σ_ϵ is the dispersion of the intrinsic ellipticity distribution. We adopt $\sigma_\epsilon = 0.32$ according to the value considered by Clampitt & Jain (2016) for a sample of background galaxies measured using SDSS data image. These quantities allow us to compute the total S/N as follows:

$$\left(\frac{S}{N} \right)^2 = \sum_i \frac{\langle \Delta\tilde{\Sigma}(r_i) \rangle^2}{\sigma_{\Delta\tilde{\Sigma}}^2(r_i)}, \tag{5}$$

where the sum runs over all the bins used to fit the profile.

3.2 Miscentred density contrast profile

McConnachie et al. (2009) define the centre of a CG as the centre of the smallest circle that contains the geometrical centre of its member galaxies. This position could be displaced from the true dark matter halo centre, leading to a flattening of the average density contrast profile and a mass underestimation.

If r_s is the projected offset in the lens plane, the azimuthally averaged $\Sigma(r)$ profile is given by the convolution (Yang et al. 2006):

$$\Sigma(r|r_s) = \frac{1}{2\pi} \int_0^{2\pi} \Sigma\left(\sqrt{r^2 + r_s^2 + 2r\, r_s \cos\theta} \right) \mathrm{d}\theta. \tag{6}$$

Since the actual offsets are not known, we adopt Johnston et al. (2007) approximation where a 2D Gaussian distribution describes this miscentring:

$$P(r_s) = \frac{r_s}{\sigma_s^2} \exp\left(-\frac{1}{2}(r_s/\sigma_s)^2 \right), \tag{7}$$

where σ_s is the width of the distribution. This value has been obtained in previous analysis of groups and cluster of galaxies, considering the brightest cluster galaxy of the system centre. George et al. (2012) reported $\sigma_s = 24.8 \pm 12$ kpc for X-ray selected groups. On the other hand, other works estimate higher values ranging from 0.2 to 0.42 h^{-1} Mpc, being higher for massive clusters (Johnston et al. 2007; van Uitert et al. 2016). The discrepancy between these results could rely on the sample properties, since X-ray selected groups may contain more relaxed systems. Taking into account the above considerations and the fact that CGs are much smaller than clusters, with typical radii of $\sim 40\, h_{70}^{-1}$ kpc, we assume $\sigma_s = 40\, h_{70}^{-1}$ kpc.

The resulting projected surface mass density for the sample can be written as

$$\Sigma_s(r) = \int_0^\infty P(r_s)\Sigma(r|r_s)\mathrm{d}r_s \tag{8}$$

and $\Delta\Sigma_s(r)$ can then be calculated with equation (2) considering that

$$\bar{\Sigma}_s(< r) = \frac{2}{r^2} \int_0^r r'\Sigma_s(r')\mathrm{d}r'.$$

The effect of this miscentring on $\Delta\Sigma(r)$ produces a suppression on the lensing signal at scales of the order of σ_s. On the outer region however, the signal remains almost unaffected.

3.3 Fitting mass density profiles

Density contrast profile $\langle \Delta \tilde{\Sigma}(r_i) \rangle$ is computed using non-overlapping concentric logarithmic annuli to preserve the S/N of the outer region, from $r_{\rm in} = 50\,h_{70}^{-1}$ kpc up to $r_{\rm out} \approx 900\,h_{70}^{-1}$ kpc, where the signal weakens. We fit this profile using two models, the singular isothermal sphere (SIS) and the Navarro, Frenk & White (NFW, 1997) profile. The SIS profile describes a relaxed spherical distribution with a constant 1D velocity dispersion, σ_V. In this model, the shear $\gamma(\theta)$ at an angular distance θ from the lens' centre is directly related to σ_V by the equation

$$\gamma(\theta) = \frac{\theta_{\rm E}}{2\theta}, \tag{9}$$

where $\theta_{\rm E}$ is the critical Einstein radius defined as

$$\theta_{\rm E} = \frac{4\pi\sigma_V^2}{c^2}\frac{1}{\langle\beta\rangle}. \tag{10}$$

From this model, we can compute the characteristic mass $M_{200} \equiv M(<R_{200})$, defined as the mass within the radius that encloses a mean density 200 times the critical density of the Universe, as in Leonard & King (2010):

$$M_{200} = \frac{2\sigma_V^3}{\sqrt{50}\,GH(z)}. \tag{11}$$

The NFW is a radial profile constructed by fitting the average halo density profile in cold dark matter numerical simulations. It depends on two parameters, R_{200} and a dimensionless concentration parameter, c_{200}, as follows:

$$\rho(r) = \frac{\rho_{\rm crit}\delta_{\rm c}}{(r/r_{\rm s})(1 + r/r_{\rm s})^2}, \tag{12}$$

where $r_{\rm s}$ is the scale radius, $r_{\rm s} = R_{200}/c_{200}$ and $\delta_{\rm c}$ is the characteristic overdensity of the halo,

$$\delta_{\rm c} = \frac{200}{3}\frac{c_{200}^3}{\ln(1 + c_{200}) - c_{200}/(1 + c_{200})}. \tag{13}$$

In order to fit this profile, we use the gravitational lensing expressions formulated by Wright & Brainerd (2000). There is a well-known degeneracy between the two parameters R_{200} and c_{200} that can be broken by combining weak and strong lensing information. Since we lack strong lensing information for CGs, we can estimate the concentration parameter with the relation $c_{200}(M_{200}, z)$, given by Duffy et al. (2011), using the M_{200} value obtained in the SIS fit and the average redshift of CGs weighted by their number of background galaxies. We use this approximation considering that the derived NFW masses are not too sensitive to this parameter given the uncertainties in the shear profile. Once the concentration is estimated, we fit the NFW profile with only one free parameter, R_{200}, and calculate M_{200}.

We derived the parameters of each mass model performing a standard χ^2 minimization:

$$\chi^2 = \sum_i^N \frac{(\langle\Delta\tilde{\Sigma}(r_i)\rangle - \Delta\tilde{\Sigma}(r_i, p))^2}{\sigma_{\Delta\tilde{\Sigma}}^2(r_i)}, \tag{14}$$

where the sum runs over the N radial bins of the profile and p is the fitted parameter ($\bar{\sigma}_V$ in the case of the SIS profile and $\bar{R}_{200}$ for the NFW model). Errors in the fitted parameters were computed according to the χ^2 dispersion. The optimal bin steps were chosen to minimize χ^2 values.

Other lensing studies consider the average density contrast profile taking into account the contribution from other neighbouring mass concentrations by introducing another halo term
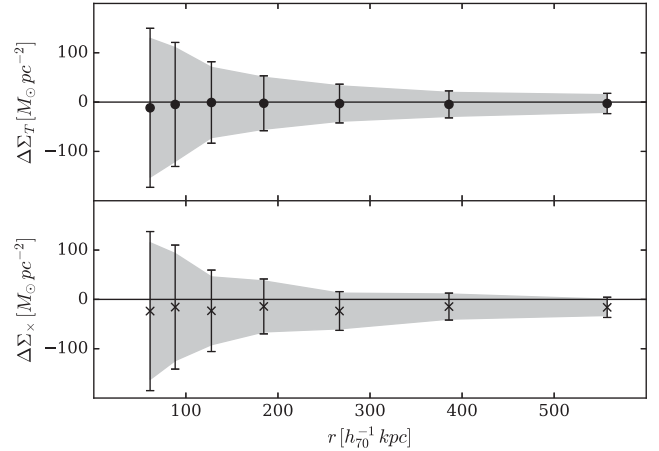

Figure 5. Averaged profiles obtained from 200 realizations using random centres for each lensing system. Upper and lower panels show profiles computed by averaging the tangential and cross ellipticity components. The shaded regions correspond to 1σ dispersion.

(e.g. Johnston et al. 2007; Leauthaud et al. 2010; Oguri & Takada 2011). In order to test our results derived up to $r_{\rm out} = 900\,h_{70}^{-1}$ kpc, we have also fitted the profiles within a significantly smaller radius ($r_{\rm out} = 500\,h_{70}^{-1}$ kpc). We find that the derived CG density contrast profiles are in good agreement within uncertainties, showing the reliability of our results.

3.4 Systematic errors and control test

Here we present the results of a control test to check the confidence of our lensing analysis. We also discuss the uncertainties regarding redshift estimation of background galaxies and the dispersion among stacked groups. We do not take into account errors regarding background sky obscuration given that this effect is negligible for SDSS (Simet & Mandelbaum 2015). The effects of miscentring are discussed in detail in Section 4.

In order to test the reliability of our measured lensing signal, we compute radial profiles using the background galaxy catalogue centred at random positions within the field of each frame. We carried out 200 realizations to look for any systematics in the density contrast profiles. In Fig. 5, we show the averaged profiles together with the dispersion of the resulting 200 realizations. The obtained profiles, using the tangential and cross ellipticity components, are both consistent with a null signal.

Given that the geometrical factor was estimated using a catalogue of photometric redshifts, based on Deep Field 1 that covers 1 square degree, we estimate the impact of cosmic variance on $\langle\beta\rangle$. We divided this field into 25 non-overlapping areas of $\sim$144 arcmin^2, assuming the average CG redshift of 0.12, and computed $\langle\beta\rangle$ for each area. The uncertainty in this parameter was estimated according to the dispersion of the 25 regions, obtaining a typical value of 10 per cent, which implies a 15 per cent error in the mass.

In order to test the stability of our results, we performed a bootstrap analysis by fitting both, SIS and NFW centred models, to 1000 samples of identical size randomly selected with reposition. The distributions of the best-fitting parameters, σ_V and R_{200}, follow approximately Gaussian distributions with dispersions lower than 10 per cent.

The uncertainties introduced by the issues discussed here are considerably lower than the errors obtained according to the χ^2
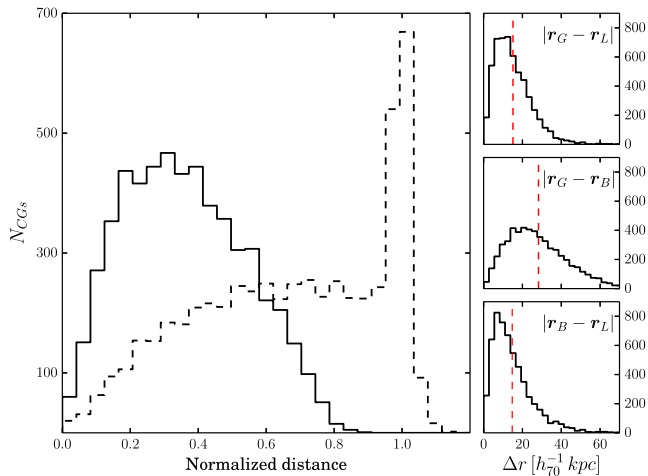
Figure 6. Left: distributions of normalized distances. The solid line corresponds to $|r_G - r_L|/R$, where r_G and r_L are the coordinates of the geometrical and luminosity-weighted centres, respectively, and R is the CG radius. The dashed line corresponds to $|r_G - r_B|/R$, where r_B is the coordinates of the brightest galaxy member. Right: distribution of centre differences in physical units. From top to bottom, $|r_G - r_L|$, $|r_G - r_B|$ and $|r_B - r_L|$. The vertical dashed lines indicate the respective mean values of the distributions.

dispersion. Nevertheless, these were considered in the final error estimation.

4 RESULTS

4.1 Centre definition analysis

In order to analyse the centre offsets with respect to those of the true dark matter haloes, we consider three different centre choices: the geometrical (GC, included in catalogue B), the coordinates of the brightest member (BC, also in catalogue B) and a geometrical centre weighted by luminosity (LC), i.e.

$$r_L = \frac{\sum r_i L_i}{\sum L_i}, \tag{15}$$

where $r_i = (\alpha, \delta)$ are the group members' celestial coordinates and L_i are their corresponding r-band luminosities. L_i were computed using CGs' redshifts and r-band magnitudes corrected by galactic extinction. We applied k-corrections to magnitudes, using Chilingarian, Melchior & Zolotukhin (2010) public code CALCK_COR.PY.[1] In Fig. 6, we show the distributions of normalized centre differences and in physical units: $|r_G - r_L|$ (where r_G is the coordinates of the geometrical centre), $|r_G - r_B|$ (where r_B is the coordinates of the brightest galaxy member) and $|r_B - r_L|$. As can be noticed, the distribution of the brightest galaxy shows a peak at the group radius given the characteristics of the identification algorithm of CGs.

The measured density profiles for the three centre choices are shown in Fig. 7. We include in this figure the fitted centred (SIS and NFW) and miscentred (SIS$_s$ and NFW$_s$) models, with their corresponding parameters and the reduced χ^2 values of each fit. Points and crosses represent the tangential and cross density contrast components averaged in annular bins, respectively.

As can be seen, there are differences in the inner region of the derived profiles. The slope of the LC centred profile presents no signs of flattening inwards ($r \lesssim 100 \, h_{70}^{-1}$ kpc), contrary to GC and

[1] Avialble at http://kcor.sai.msu.ru/getthecode/

BC centred profiles. Nevertheless, according to $\chi^2_{\rm red}$, both profiles are well described by a miscentred model as well as by a centred one. In general, derived masses from both centred and miscentred profiles are in mutual agreement taking into account the uncertainties, while larger differences are observed for SIS masses. Given that the SIS profile is more sensitive to centre definition, we have compared the obtained χ^2 of both, centred and miscentred, SIS fitted profiles (see Fig. 7), and therefore we choose the LC as the gravitational potential centre. In Table 1, we summarize our results adding the errors discussed in Section 3.4.

The model that best describes the LC centred profile is the centred SIS yielding an average velocity dispersion of $\sigma_V = 270 \pm 40 \, {\rm km \, s^{-1}}$, which corresponds to $M_{200} = 17 \pm 8 \times 10^{12} \, h_{70}^{-1} \, {\rm M_\odot}$. Since the haloes of CGs are expected to have undergone significant contraction due to the baryonic cooling and collapse, a SIS profile can be a suitable alternative model to NFW, to describe the mass distribution of these low-mass systems. It should be noted, however, that the estimated SIS and NFW masses are in good agreement within a $\sim$10 per cent factor as in previous works (Gonzalez et al. 2015, 2016). For the rest of the analysis, we use these fitted parameters to compare them with dynamical estimates and to study variations in the total sample.

4.2 Dependence of the lensing signal on CG physical properties

We studied how CG average lensing mass varies with respect to three parameters: physical radius, R, surface brightness, μ, and average concentration index weighted by luminosity, C_L. We defined C_L for a group as

$$C_L = \frac{\sum c_i L_i}{\sum L_i}, \tag{16}$$

where c_i is the individual concentration index of member galaxies defined as the ratio of the radii enclosing 90 and 50 per cent of the Petrosian flux, i.e. $c_i = r_{90}/r_{50}$. For each parameter, we divided our sample into two equal-sized subsamples according to the median value of the parameter distribution. In Fig. 8, we plot these parameters' distributions together with their respective subsamples' distributions.

In Table 2, we summarize the results of this analysis. To test the significance of these results, we performed a jackknife resampling technique by randomly choosing 1000 subsamples taking 50 per cent of the groups. From this analysis, we obtained Gaussian distributions for the fitted parameters with dispersions of $30 \, {\rm km \, s^{-1}}$ and 0.08 Mpc for σ_V and R_{200}, respectively. We find no significant variation of the fitted parameters for the R and μ subsamples, since they are in good agreement taking into account the errors. However, for the C_L subsamples, the resulting parameters differ by $\sim 2\sigma$ considering the jackknife dispersion.

The concentration index is an indicator of galaxy morphology, where late-type galaxies tend to have lower c_i values than early-type. Thus, groups with lower and higher C_L are expected to be dominated by late- and early-type galaxies, respectively. The detection of a higher lensing signal for groups with higher C_L values could be influenced by a lower fraction of interlopers. Given that CGs are expected to have a greater fraction of early-type members, by selecting CGs with low C_L we could be including more systems with interlopers and, thus, reducing the lensing signal. As a matter of fact, this cut in concentration modifies the distribution of surface brightness: higher C_L groups tend to be brighter than lower C_L groups (see Fig. 8). As mentioned before, the fraction of
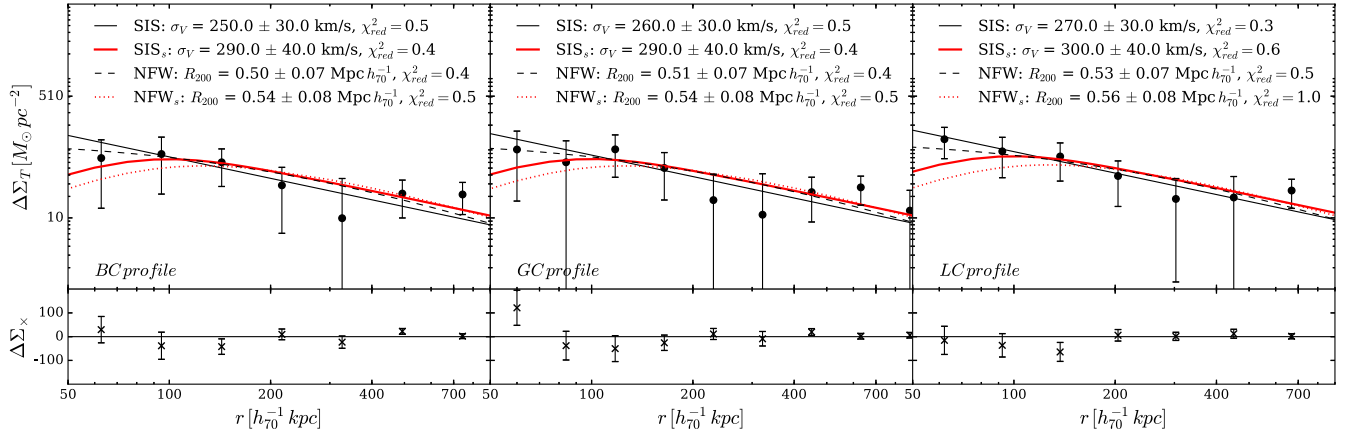
Figure 7. Average density contrast $\Delta\Sigma(r)$ profile of CG sample for each centre: BC (left), GC (middle) and LC (right). Solid thin and thick lines represent the best centred and miscentred SIS fits, respectively; dashed and dotted lines represent the best centred and miscentred NFW fits, respectively. The lower panels of each plot show the profile obtained using the cross component of the background galaxies" ellipticity. Error bars are computed according to equation (4). Parameter errors consider only the fitting uncertainties and do not include those discussed in Section 3.4.

Table 1. CG results. Columns: (1) centre choice; (2) and (3) results from the centred SIS fit: velocity dispersion and M_{200}^{SIS}; (4) and (5) results from the miscentred SIS fit: velocity dispersion and M_{200}^{SIS}; (6)–(8) results from the centred NFW fit: c_{200} estimated with the centred M_{200}^{SIS} (see the text for details), R_{200} and M_{200}^{NFW}; (9) and (10) results from the miscentred NFW fit: c_{200} estimated with the miscentred M_{200}^{SIS} (see the text for details), R_{200} and M_{200}^{NFW}; (11) S/N ratio as defined in equation (5). σ_V, R_{200} and M_{200} are in units of $\mathrm{km\,s^{-1}}$, h_{70}^{-1} Mpc and $10^{12}\,h_{70}^{-1}\,\mathrm{M_\odot}$, respectively.

Centre	SIS		SIS$_s$		NFW			NFW$_s$			S/N
	σ_V	M_{200}	σ_V	M_{200}	c_{200}	R_{200}	M_{200}	c_{200}	R_{200}	M_{200}	
BC	250 ± 60	14 ± 8	290 ± 60	21 ± 13	4.54 ± 0.23	0.50 ± 0.11	16 ± 11	4.38 ± 0.22	0.54 ± 0.12	21 ± 13	4.0
GC	260 ± 50	15 ± 10	290 ± 60	21 ± 13	4.51 ± 0.22	0.51 ± 0.11	17 ± 11	4.38 ± 0.22	0.54 ± 0.12	21 ± 14	4.2
LC	270 ± 40	17 ± 8	300 ± 60	24 ± 12	4.45 ± 0.21	0.53 ± 0.10	19 ± 11	4.33 ± 0.21	0.56 ± 0.11	22 ± 13	4.6

interlopers declines as brighter groups are considered (Mc-Connachie et al. 2008), and since the estimated parameters are in agreement for both μ subsamples, this result suggests that a cut in C_{L} may be more efficient than a cut in μ in order to reduce the contamination in the CG sample. This is also evident from the observed relations between $\langle C_{\mathrm{L}} \rangle$ versus N_z, and $\langle C_{\mathrm{L}} \rangle$ versus N_z/N_{members}. N_z is the number of member galaxies with available spectroscopy, and N_{members} is the total number of members (we restrict to groups with a maximum line-of-sight velocity difference between pairs of members, $\max(\Delta v) < 1000\,\mathrm{km\,s^{-1}}$, a usual criterion to minimize interlopers; Hickson et al. 1992; McConnachie et al. 2009). As can be seen in Fig. 9, groups with higher C_{L} tend to have higher N_z and N_z/N_{members} values, making them more reliable. In Fig. 10, we show images for both subsamples together with their respective average density contrast profiles. By selecting CGs dominated by early-type galaxies, the systems tend to be more massive and evidence a more evolved structure.

4.3 Comparison with dynamical estimates

Given that the σ_V parameter derived from the weak lensing analysis can be directly compared with dynamical estimates, we have analysed the redshift distribution of CGs' member galaxies in order to estimate the dynamical velocity dispersion, $\sigma_{V,\mathrm{dyn}}$. With this aim, we consider only CGs having three or more members with redshift information and, as before, we discard those with $\max(\Delta v) > 1000\,\mathrm{km\,s^{-1}}$. From our sample of 5568 CGs, only 61 satisfy these requirements. We find a median dynamical velocity dispersion $\sigma_{V,\mathrm{dyn}} = 224 \pm 13\,\mathrm{km\,s^{-1}}$, where the uncertainty

corresponds to the 1σ standard deviation derived from 1000 bootstrap resamplings. This value is in good agreement with other dynamical estimates for CGs: $\simeq 200\,\mathrm{km\,s^{-1}}$ (Hickson et al. 1992; Duplancic et al. 2015; Sohn et al. 2015) and $\simeq 230\,\mathrm{km\,s^{-1}}$ (McConnachie et al. 2009).

Since gravitational lensing allows the measurement of the mass distribution at large angular distances from the centre, one would expect that CG lensing inferred velocity dispersions could be higher than those derived from their core's dynamics. It should also be taken into account that the presence of dynamical friction among highly interacting group members could further reduce their velocity dispersion. Nevertheless, the weak lensing estimate of $\sigma_V = 270 \pm 40\,\mathrm{km\,s^{-1}}$, although slightly higher, mutually agrees with dynamical determinations within 1σ.

Using the same criteria, we also estimated the dynamical velocity dispersion for both C_{L} subsamples. For groups with higher C_{L} values, we find $\sigma_{V,\mathrm{dyn}} = 238 \pm 15\,\mathrm{km\,s^{-1}}$, while for groups with lower C_{L} we find $\sigma_{V,\mathrm{dyn}} = 190 \pm 22\,\mathrm{km\,s^{-1}}$. These results show the same tendency as the aforementioned weak lensing estimates, reinforcing their interpretation.

5 SUMMARY

In this work, we analysed a sample of CGs from McConnachie et al. (2009) catalogue B using weak lensing stacking techniques. We derive the average density contrast profile of the composite system for three centre definitions: the geometrical centre, the brightest galaxy member and a luminosity-weighted centre. Measured profiles were fitted using centred and miscentred, SIS and NFW, density models.
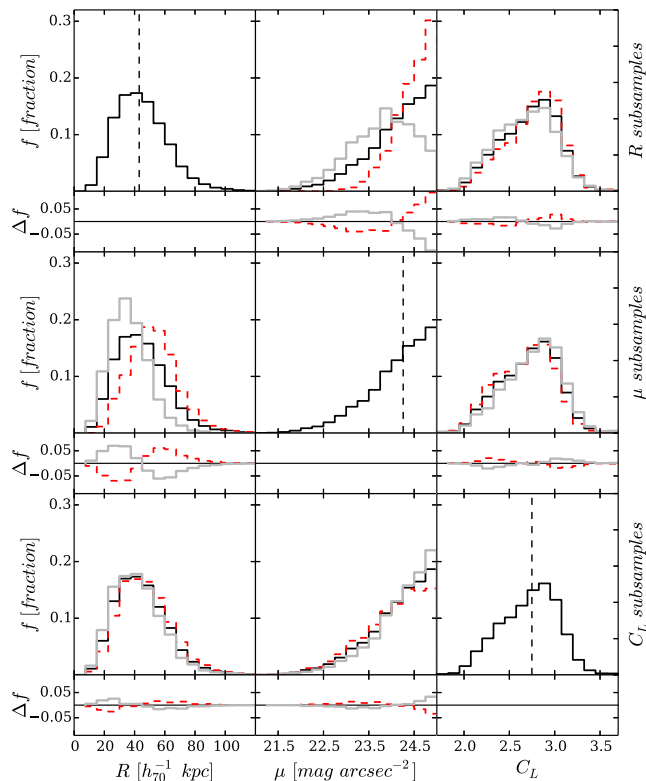
Figure 8. Parameter variation for each subsample. Columns: (1) physical radius, R; (2) surface brightness, μ; (3) weighted concentration index, C_L (see the text for definition). Rows: (1) R subsamples; (2) μ subsamples; (3) C_L subsamples. All distributions were normalized to have the same area. The solid black lines correspond to the complete sample; the dashed and grey lines correspond to the higher and lower subsamples, respectively. Below each panel, we show the residuals between the complete sample distribution and each subsample.

Table 2. Subsample results. Columns: (1) selection criterion according to the median value of each distribution; (2) velocity dispersion from the SIS fit (km s^{-1}); (3) and (4) fixed c_{200} and estimated R_{200} (h_{70}^{-1} Mpc) from the NFW fit.

Subsample	SIS	NFW	
	σ_V	c_{200}	R_{200}
$R > 43\ h_{70}^{-1}$ kpc	270 ± 50	4.44 ± 0.24	0.49 ± 0.13
$R < 43\ h_{70}^{-1}$ kpc	260 ± 60	4.50 ± 0.25	0.51 ± 0.13
$\mu > 24.25$ mag arcsec^{-2}	290 ± 50	4.37 ± 0.22	0.58 ± 0.13
$\mu < 24.25$ mag arcsec^{-2}	240 ± 60	4.59 ± 0.27	0.45 ± 0.13
$C_L > 2.75$	300 ± 50	4.33 ± 0.21	0.56 ± 0.13
$C_L < 2.75$	220 ± 60	4.70 ± 0.31	0.43 ± 0.14

Luminosity-weighted centres were selected as the best description of the true dark matter halo centres.

We also studied the lensing signal dependence on physical parameters (radius, surface brightness and concentration index of galaxy members) of the CGs. We did not observe a significant difference between the fitted parameters for subsamples defined according to group radius and surface brightness cuts. Nevertheless, CGs composed of galaxies with larger c_i show a stronger lensing signal. This could be explained by a lower number of interlopers, as well as by a trend to include more massive and evolved systems. We argue that considering groups with higher concentration index weighted
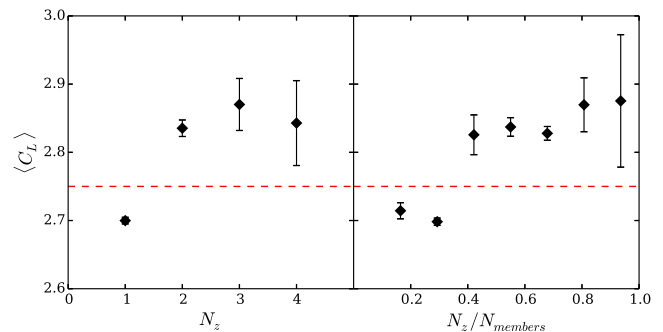

Figure 9. Variation of the average C_L with the number of members with spectroscopic redshift (left) and with the respective fraction (right). The dashed line marks the median value of C_L used to divide the sample.

by luminosity could be efficient in order to increase the fraction of genuine CGs in the sample.

The resulting velocity dispersion derived from the SIS profile was compared to the dynamical estimate obtained from spectroscopic information of member galaxies. Although the lensing estimate is slightly higher, both results are in good agreement within uncertainties.

This work provides the first lensing analysis of a sample of CGs based on SDSS images. Our results, in agreement with other dynamical estimates, give hints on the mass distribution and dependence on CG properties. In a forthcoming paper, we will consider in detail mass-to-light ratio and a comparison to simulations.
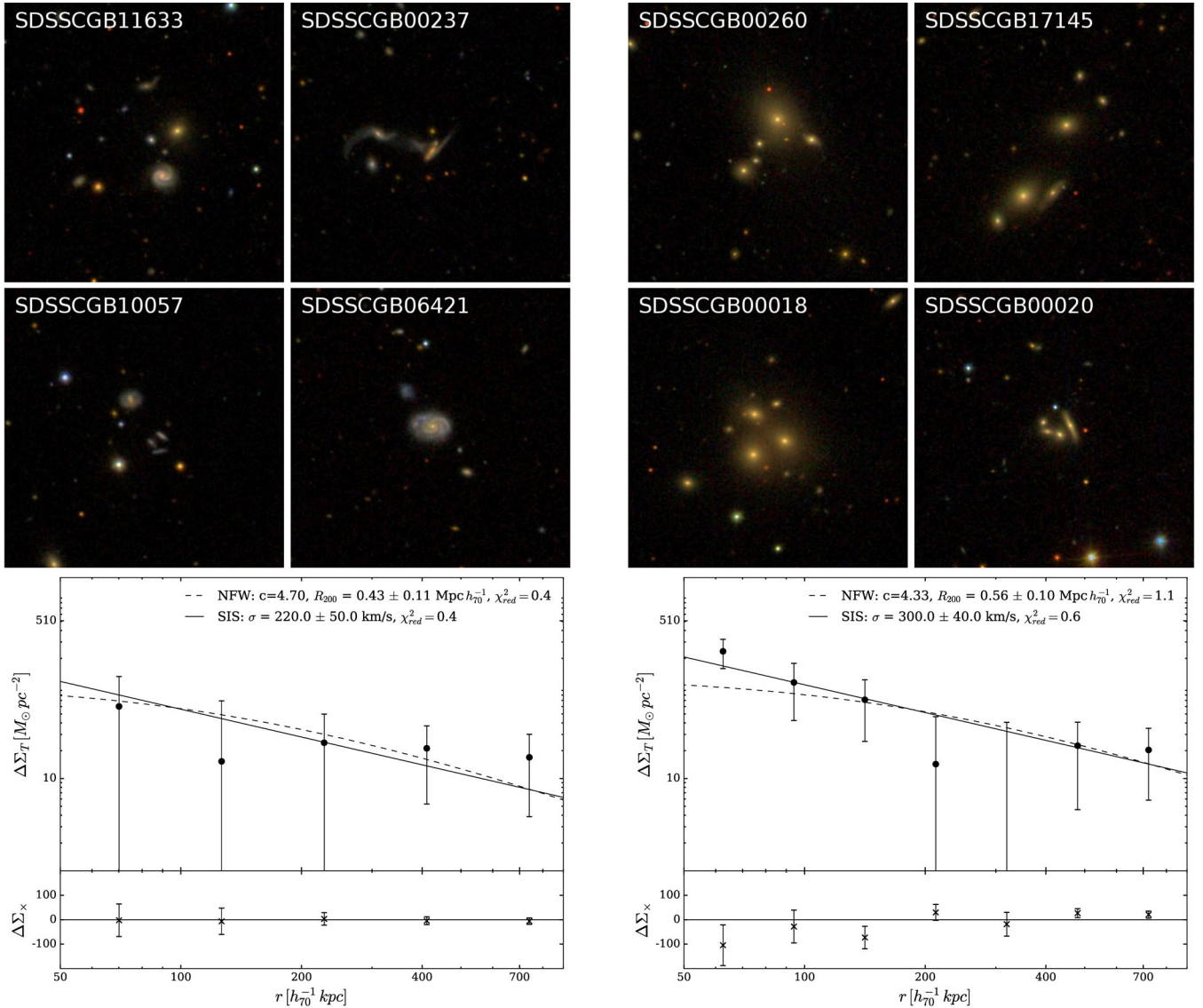
ACKNOWLEDGEMENTS

Figure 10. Example of CGs present in both C_L subsamples accompanied by their respective density contrast profile. As in Fig. 7, parameter errors consider only the fitting uncertainties and do not include those discussed in Section 3.4. The four images on the left, and the profile below them, correspond to the sample with lower C_L values. The remaining figures on the right-hand side correspond to systems with higher C_L values. Images were obtained from the SDSS Navigate Tool.

REFERENCES

Adelman-McCarthy J. K. et. al., 2008, ApJS, 175, 297

Ahn C. P. et al., 2014, ApJS, 211, 17

Alam S. et al., 2015, ApJS, 219, 12

Allam S. S., Tucker D. L., 2000, Astron. Nachr., 321, 101

Athanassoula E., Makino J., Bosma A., 1997, MNRAS, 286, 825

Barnes J., 1984, MNRAS, 208, 873

Barnes J., 1985, MNRAS, 215, 517

Barnes J. E., 1989, Nature, 338, 123

Bartelmann M., 1995, A&A, 303, 643

Barton E., Geller M., Ramella M., Marzke R. O., da Costa L. N., 1996, AJ, 112, 871

Bertin E., Arnouts S., 1996, A&AS, 117, 393

Bode P. W., Cohn H. N., Lugger P. M., 1993, ApJ, 416, 17

Bridle S. L., Kneib J.-P., Bardeau S., Gull S. F., 2002, in Natarajan P., ed., The Shapes of Galaxies and Their Dark Halos. World Scientific Press, Singapore, p. 38

Chilingarian I. V., Melchior A.-L., Zolotukhin I. Y., 2010, MNRAS, 405, 1409

Clampitt J., Jain B., 2016, MNRAS, 457, 4135

Clowe D., Luppino G. A., Kaiser N., Gioia I. M., 2000, ApJ, 539, 540

Coupon J. et al., 2009, A&A, 500, 981

de Carvalho R. R., Gonçalves T. S., Iovino A., Kohl-Moreira J. L., Gal R. R., Djorgovski S. G., 2005, AJ, 130, 425

Diaferio A., Geller M. J., Ramella M., 1994, AJ, 107, 868

Duffy A. R., Schaye J., Kay S. T., Dalla Vecchia C., 2011, MNRAS, 415, L85

Duplancic F., Alonso S., Lambas D. G., O'Mill A. L., 2015, MNRAS, 447, 1399

Fischer P., 1999, AJ, 117, 2024

Foëx G., Motta V., Limousin M., Verdugo T., More A., Cabanac R., Gavazzi R., Muñoz R. P., 2013, A&A, 559, A105

Foëx G., Motta V., Jullo E., Limousin M., Verdugo T., 2014, A&A, 572, A19

George M. R. et al., 2012, ApJ, 757, 2

Gonzalez E. J., Foëx G., Nilo Castellón J. L., Domínguez Romero M. J., Alonso M. V., García Lambas D., Moreschi O., Gallo E., 2015, MNRAS, 452, 2225

Gonzalez E. J., Rodriguez F., García Lambas D., Merchán M., Foëx G., Chalela M., 2016, MNRAS, 465, 1348

Governato F., Bhatia R., Chincarini G., 1991, ApJ, 371, L15

Hickson P., 1982, ApJ, 255, 382

Hickson P., Mendes de Oliveira C., Huchra J. P., Palumbo G. G., 1992, ApJ, 399, 353

Hoekstra H., 2007, MNRAS, 379, 317

Hoekstra H., Franx M., Kuijken K., Squires G., 1998, ApJ, 504, 636

Iovino A., 2002, AJ, 124, 2471

Johnston D. E., Sheldon E. S., Tasitsiomi A., Frieman J. A., Wechsler R. H., McKay T. A., 2007, ApJ, 656, 27

Karachentsev I. D., 2005, AJ, 129, 178

Leauthaud A. et al., 2010, ApJ, 709, 97

Leonard A., King L. J., 2010, MNRAS, 405, 1854

McConnachie A. W., Ellison S. L., Patton D. R., 2008, MNRAS, 387, 1281

McConnachie A. W., Patton D. R., Ellison S. L., Simard L., 2009, MNRAS, 395, 255

Mamon G. A., 1986, ApJ, 307, 426

Mamon G. A., 1987, ApJ, 321, 622

Mandelbaum R., Seljak U., Cool R. J., Blanton M., Hirata C. M., Brinkmann J., 2006, MNRAS, 372, 758

Mendel J. T., Ellison S. L., Simard L., Patton D. R., McConnachie A. W., 2011, MNRAS, 418, 1409

Mendes de Oliveira C., Giraud E., 1994, ApJ, 437, L103

Meylan G., Jetzer P., North P., Schneider P., Kochanek C. S., Wambsganss J., eds, 2006, Gravitational Lensing: Strong, Weak and Micro. Springer, Berlin, p. 336

Navarro J. F., Frenk C. S., White S. D. M., 1997, ApJ, 490, 493

Oguri M., Takada M., 2011, Phys. Rev. D, 83, 023008

Pompei E., Iovino A., 2012, A&A, 539, A106

Ponman T. J., Bourner P. D. J., Ebeling H., Böhringer H., 1996, MNRAS, 283, 690

Prandoni I., Iovino A., MacGillivray H. T., 1994, AJ, 107, 1235

Rood H. J., Struble M. F., 1994, PASP, 106, 413

Rykoff E. S. et al., 2008, MNRAS, 387, L28

Sheldon E. S. et al., 2009, ApJ, 703, 2217

Simet M., Mandelbaum R., 2015, MNRAS, 449, 1259

Sohn J., Hwang H. S., Geller M. J., Diaferio A., Rines K. J., Lee M. G., Lee G.-H., 2015, J. Korean Astron. Soc., 48, 381

Spinelli P. F., Seitz S., Lerchster M., Brimioulle F., Finoguenov A., 2012, MNRAS, 420, 1384

van Uitert E., Gilbank D. G., Hoekstra H., Semboloni E., Gladders M. D., Yee H. K. C., 2016, A&A, 586, A43

Wright C. O., Brainerd T. G., 2000, ApJ, 534, 34

Yang X., Mo H. J., van den Bosch F. C., Jing Y. P., Weinmann S. M., Meneghetti M., 2006, MNRAS, 373, 1159

York D. G. et al., 2000, AJ, 120, 1579

This paper has been typeset from a TEX/LATEX file prepared by the author.